Showcasing research from Professor Zhiping Luo's laboratory, Fayetteville State University, North Carolina, USA.

Computational–experimental assessment of transition-metal doping of Co_3O_4 for acidic oxygen evolution reaction with balanced activity and stability

Density-functional theory (DFT) screening of fourth-row transition-metal-doped Co_3O_4 for acidic OER establishes joint activity–stability descriptors and identifies chromium as an optimal dopant balancing performance and durability. Guided by computation, experiments on Cr-doped samples validated the dopant's high activity and stability. This work offers a broadly applicable strategy to discover effective dopants for oxide OER catalysts in acidic media.

Image reproduced by permission of Zhiping Luo from *J. Mater. Chem. A*, 2026, **14**, 3297.

Artwork generated using Adobe Firefly.

As featured in:

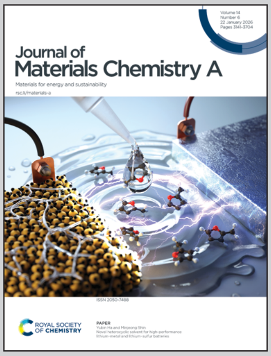

See Zhiping Luo *et al.*,
J. Mater. Chem. A, 2026, **14**, 3297.

ROYAL SOCIETY
OF **CHEMISTRY**

rsc.li/materials-a

Registered charity number: 207890

Journal of
Materials Chemistry A

ROYAL SOCIETY
OF CHEMISTRY

PAPER

View Article Online
View Journal | View Issue

Cite this: *J. Mater. Chem. A*, 2026, **14**, 3297

Computational–experimental assessment of transition-metal doping of Co_3O_4 for acidic oxygen evolution reaction with balanced activity and stability

Sivasankara Rao Ede,[ab] Hanna M. Paige,[a] Jett Wu,[a] Chandra M. Adhikari,[a] Amar S. Kumbhar,[c] Shubo Han[a] and Zhiping Luo*[a]

Acidic water oxidation using earth-abundant oxides remains challenging because of sluggish kinetics and poor stability under oxygen evolution reaction (OER) conditions. Herein, density functional theory was used to systematically screen fourth-row transition-metal dopants in Co_3O_4 and establish joint activity–stability descriptors. It was found that early-series dopants improve the lattice thermodynamic stability, while chromium maximizes the electrochemical stability. Enhanced OER activity correlated with moderate values of the d-band center, metal–oxygen covalency, and integrated crystal orbital Hamiltonian population, indicating an optimal bonding regime. Chromium has emerged as an optimal dopant, striking a balance between stability and activity of the catalyst. Guided by these predictions, experiments demonstrated that 10% Cr-doped Co_3O_4 exhibited excellent OER performance, achieving an overpotential of 366 mV at 10 mA cm^{-2} in 0.5 M H_2SO_4 and improving durability 2.7-fold, with only an 11 mV increase in overpotential after extended testing. This combined computational–experimental study outlines a generalizable pathway for identifying effective dopants for oxide catalysts in acidic OER by concurrently optimizing stability and catalytic activity.

Received 7th October 2025
Accepted 18th November 2025

DOI: 10.1039/d5ta08166a

rsc.li/materials-a

1 Introduction

Electrochemical water oxidation plays a crucial role in clean energy technologies, including hydrogen production through water electrolysis, electricity generation *via* fuel cells, energy storage using metal–air batteries, and environmental remediation.[1] The presence of efficient catalysts greatly facilitates the water oxidation.[2–5] Generally, water electrolysis is classified into three types based on the electrolyte medium: solid-oxide electrolysis, alkaline electrolysis, and proton exchange membrane water electrolysis (PEMWE).[6] Among these, PEMWE has attracted significant attention owing to its advantages, including rapid response to power fluctuations, higher current density, high efficiency, high-purity hydrogen, and low gas crossover.[6,7] In PEMWE, the hydrogen evolution reaction (HER) occurs at the cathode and the oxygen evolution reaction (OER) at the anode. However, the OER under acidic conditions poses a significant bottleneck for PEMWE due to three key challenges: catalyst dissolution, sluggish water dissociation, and weak binding of OER intermediates (adsorbates).[8,9] Consequently, improving the efficiency of PEMWE electrolysis depends critically on the development of efficient, cost-effective, and durable OER catalysts that perform well in acidic environments.

In the development of PEMWE anode OER catalysts, Ir- and Ru-based catalysts have been considered the most suitable for PEMWE electrolyzers due to their high activity and stability.[10,11] However, the high cost and scarcity of these metals limit their large-scale applications. Developing PEMWE catalysts based on earth-abundant elements is thus of great significance. Various noble metal-free catalysts have been reported, including metal oxides and their hybrids,[12,13] carbons,[14] and metal–organic frameworks.[15] Among the metal oxides and their hybrids, cobalt oxide (Co_3O_4) has been recognized as a promising catalyst,[16] with a theoretical catalytic overpotential comparable to that of RuO_2.[17] Co_3O_4 has a spinel structure, in which Co^{3+} ions occupy octahedral sites and Co^{2+} ions occupy tetrahedral sites. This mixed-valence structure offers opportunities to tune their intrinsic electronic properties through doping or other structural engineering with transition-metal (TM) cations.[16]

Various TM elements have been used to dope Co_3O_4, enhancing its OER activity in alkaline solutions. Among them, Fe doping has been shown to improve performance in Co-based oxides significantly.[18–21] For instance, Fe doping reduced the overpotential (η_{10}) at 10 mA cm^{-2} by 160 mV,[18] and Fe-doped

---

[a] Department of Chemistry, Physics, and Materials Science, Fayetteville State University, Fayetteville, North Carolina 28301, USA. E-mail: zluo@uncfsu.edu

[b] Department of Chemistry, Koneru Lakshmaiah Education Foundation, Green Fields, Vaddeswaram, Andhra Pradesh 522302, India

[c] Chapel Hill Analytical and Nanofabrication Laboratory, University of North Carolina, Chapel Hill, North Carolina 27599, USA

Co_3O_4 nanosheets achieved an η_{10} of 262 mV.[19] Similarly, Ni doping at 4 wt% lowered η_{10} to 240 mV.[22] Lin and McCrory doped Cr into $Co_{3-x}Cr_xO_4$ and optimized the doping level at $x = 0.75$ (25%), achieving an overpotential of $\eta_{10} = 350$ mV.[23] Banerjee *et al.* compared the effects of Ni, Fe, and Cr doping into Co_3O_4 for OER in an alkaline medium, finding that Cr (146 mV) slightly outperformed Ni (148 mV) and Fe (150 mV).[24] More recently, doping Co_3O_4 with various TMs revealed that Fe, Ni, and In doping reduced the overpotentials in alkaline media, whereas Al and Ga doping increased them.[25]

TM-based oxide catalysts typically exhibit excellent water oxidation performance at alkaline and near-neutral pH conditions; however, they often underperform in acidic environments due to their susceptibility to corrosion. However, Co_3O_4 has demonstrated notable structural stability and catalytic activity under acidic conditions.[26–28] In recent years, extensive efforts have been made to enhance the intrinsic catalytic activity of Co_3O_4 through doping,[29] primarily with TMs. While noble metal dopants such as Ir,[30–32] Ru,[33–36] and Ag[37] have shown high performance in acidic OER, there is growing interest in identifying effective dopants among earth-abundant elements. For example, Fe doping reduced the η_{10} from 359 to 295 mV in Co_3O_4 nanosheets,[38] while Ni doping reduced the η_{10} from 381 to 330 mV in Co_3O_4 nanofibers in 0.5 M H_2SO_4.[39] Cr-doped Co_3O_4 nanoparticles grown on carbon paper exhibited a reduction in the η_{10} from 385 to 333 mV.[40] Additionally, Sn doping decreased the η_{10} from 524 to 496 mV, whereas Mn and Sb doping increased the η_{10} to 602 and 606 mV, respectively.[41]

The search for efficient acidic OER catalysts is often pursued *via* dopant-by-dopant screening; however, OER performance depends on multiple coupled factors, including catalyst composition, substrate, and synthesis conditions, making it challenging to isolate the pure dopant effects. To address this, we present a general strategy based on density functional theory (DFT) computations to identify dopants that balance high catalytic activity with chemical stability under acidic OER conditions. We emphasize that searches should jointly consider both the activity and structural stability. Through a systematic evaluation of first-row (Sc–Zn) TM doping in Co_3O_4, we identified chromium (Cr) as the optimal candidate, achieving a favorable tradeoff between stability and activity. Guided by these computational insights, we experimentally doped Cr^{3+} into crystalline Co_3O_4 nanoparticles and assessed their OER performance in 0.5 M H_2SO_4. Among the various doping levels tested, the 10% Cr compound exhibited superior OER activity compared to the pristine material and samples doped with 5%, 20%, and 30% Cr. This study demonstrates a generalizable approach for discovering effective dopants by jointly optimizing their stability and OER activity.

2 Computational and experimental methods

2.1 Computational methods

First-principles calculations were performed using the Vienna *Ab initio* Simulation Package (VASP) based on DFT.[42,43] The interactions between ions and electrons were treated using the Projector Augmented Wave (PAW) method,[44] and the exchange–correlation energy was approximated using the Perdew–Burke–Ernzerhof (PBE) functional.[45] All calculations used a plane-wave cutoff energy of 520 eV. For the bulk phase, a Monkhorst–Pack $4 \times 4 \times 4$ *k*-point mesh was employed. For the slab models, geometry optimizations were performed using a $4 \times 4 \times 2$ mesh, followed by single-point energy calculations using an $8 \times 8 \times 1$ mesh. To account for the van der Waals forces, we applied the DFT-D3 Becke–Johnson (BJ) damping correction. The self-consistent field convergence threshold was set at 1×10^{-5} eV, and the convergence force threshold was set to 0.02 eV Å^{-1}. To account for the strong electron correlations in the transition metals, we employed a simplified LSDA + U approach, where only the effective Hubbard parameter $U_{\text{eff}} = U - J$ was used.[46] The values of U_{eff}, along with the initial magnetic moments for spin-polarized calculations, are provided in Table S1.

In our modelling, elements with a valence of 3+ or higher occupy the Co^{3+} octahedral site, and elements with a valence of 2+ occupy the Co^{2+} tetrahedral site. No additional vacancies or point defects are created for charge compensation. For aliovalent dopants, we likewise use charge-neutral supercells, with charge compensation occurring electronically *via* charge redistribution.

Many OER descriptors have been reported in the literature.[47] In this work, we use the binding energy, d-band center, covalency, and Crystal Orbital Hamilton Population (COHP) as descriptors and establish volcano-like relationships in the TM-doped Co_3O_4 system, obtaining consistent trends across these different descriptors. The COHP calculation was conducted using the Lobster program,[48] and the input file, lobstering, is shown in Table S2.

2.2 Experimental methods

2.2.1 Materials and synthesis. Chromium(III) nitrate nonahydrate and cobalt(II) nitrate hexahydrate were obtained from Sigma-Aldrich, and ammonia solution (28–30 vol%), citric acid (CA), and ethylenediaminetetraacetic acid (EDTA) were procured from VWR International. All chemicals were used as received without further purification. Pristine and Cr-doped Co_3O_4 compounds were synthesized using sol–gel and combustion methods. Initially, the nitrate salts of cobalt and chromium were dissolved in 75 mL of distilled water at room temperature. The stoichiometric ratio of Co to Cr varied according to the desired compound composition. After the complete dissolution of the nitrate salts, chelating agents, such as EDTA and CA, were added. The solution was adjusted to pH 9, and the mixture was stirred for 12 h at room temperature. The resulting mixture was washed thrice with distilled water and ethanol, and then dried at 60 °C for 5 h. Finally, the dried powder was annealed at 400 °C for 3 h in air, with a ramp rate of 5 °C min^{-1} (Fig. S1).

2.2.2 Characterizations. X-ray photoelectron spectroscopy (XPS) analyses were performed using two different instruments: Thermo Scientific ESCALAB 250Xi and Kratos AXIS-ULTRA DLD-600W. X-ray diffraction (XRD) patterns were recorded using a Rigaku MiniFlex 600 X-ray diffractometer equipped with a Cu Kα radiation source. Transmission electron microscopy (TEM) was performed on an FEI Talos F200X TEM/STEM instrument operated at 200 kV.

2.2.3 Electrochemical measurements. Carbon cloth was used as a conductive support for fabricating the working electrodes. Before use, it was cleaned with a 30% ethanol solution in an ultrasonic bath and subsequently dried in an oven at 80 °C. The active material was then coated onto a 0.5 cm^2 area of the carbon cloth using a 10% polyvinylidene fluoride (PVDF) binder dissolved in *N*-methyl-2-pyrrolidone. The approximate loading of the active material was maintained at 1 mg.

All electrochemical measurements were performed using a CHI 760E electrochemical workstation. Linear sweep voltammetry (LSV) was conducted at a scan rate of 2 mV s^{-1} following five cyclic voltammetry (CV) scans at a scan rate of 100 mV s^{-1}. LSV plots were used to derive Tafel plots, and the electrochemical double-layer capacitance (C_{dl}) was determined by performing CV measurements at varying scan rates (10–125 mV s^{-1}). Electrochemical impedance spectroscopy (EIS) measurements were conducted in the frequency range of 1 kHz to 1 Hz with an amplitude of 5 mV. Mercury/mercury sulfate (Hg/Hg$_2$SO$_4$) and carbon cloth were used as the reference and counter electrodes, respectively. The electrochemical data were fully IR-compensated and converted to the reversible hydrogen electrode (RHE) scale by calibrating the Hg/Hg$_2$SO$_4$ reference electrode using the formula

$$E_{vs.\ \text{RHE}} = E_{vs.\ \text{Hg/Hg}_2\text{SO}_4} + E^0_{\text{Hg/Hg}_2\text{SO}_4} + 0.059 \times \text{pH} \tag{1}$$

for OER in 0.5 M H$_2$SO$_4$.

3 Results and discussion

3.1 Computational results and discussion

First, we evaluated the effects of doping on stability from the perspective of surface energy. Surface energy is the energy required to create a unit area of surface from the bulk material, and a lower surface energy indicates greater thermodynamic stability of the slab under OER conditions.[49,50] The pristine bulk Co$_3$O$_4$ material has a stoichiometric composition of Co$_{24}$O$_{32}$ in a unit cell. The energy required to form a slab consisting of Co$_{22}$O$_{32}$, corresponding to the surface energy, is expressed as:

$$\begin{aligned}\gamma &= \frac{1}{2A}\left[E_{\text{pristine slab}} - \frac{22}{24}E_{\text{pristine bulk}} - \left(32 - \frac{22}{24}\times 32\right)\mu_{\text{O}}\right]\\ &= \frac{1}{2A}\left[E_{\text{pristine slab}} - \frac{11}{12}E_{\text{pristine bulk}} - \frac{8}{3}\mu_{\text{O}}\right]\end{aligned} \tag{2}$$

Here, μ denotes the chemical potential, and A is the slab surface area. The energies E of the pristine slab and bulk were calculated as their ground-state energies using DFT. The chemical potential of oxygen μ_{O} is set by using $\frac{1}{2}E_{\text{O}_2}$ as a zero reference,

$$\mu_{\text{O}} = \tfrac{1}{2}E_{\text{O}_2} + \Delta\mu \tag{3}$$

Accordingly, the energy to form M-doped slab Co$_{21}$MO$_{32}$ from M-doped bulk Co$_{23}$MO$_{24}$ is

$$\begin{aligned}\gamma &= \frac{1}{2A}\left[E_{\text{doped slab}} - \frac{21}{23}E_{\text{doped bulk}} - \left(1 - \frac{21}{23}\right)\mu_{\text{M}} - \left(32 - \frac{21}{23}\times 32\right)\mu_{\text{O}}\right]\\ &= \frac{1}{2A}\left[E_{\text{doped slab}} - \frac{21}{23}E_{\text{doped bulk}} - \frac{2}{23}\mu_{\text{M}} - \frac{64}{23}\mu_{\text{O}}\right]\end{aligned} \tag{4}$$

Here, μ_{M} is obtained from its oxide. For example, μ_{Cr} is obtained from its oxide Cr$_2$O$_3$,

$$\mu_{\text{Cr}} = \frac{E_{\text{Cr}_2\text{O}_3} - 3\mu_{\text{O}}}{2} \tag{5}$$

Thus,

$$\gamma = \frac{1}{2A}\left[E_{\text{doped slab}} - \frac{21}{23}E_{\text{doped bulk}} - \frac{1}{23}E_{\text{Cr}_2\text{O}_3} - \frac{61}{23}\mu_{\text{O}}\right] \tag{6}$$

The slab model consists of seven atomic layers, symmetrically arranged about the central layer, with two exposed surfaces. For simplicity, we dope only one M atom on the top surface. The resulting doping level is approximately 4.5% (1/22) for the whole model, or about 9.1% on the active surface side.

The surface energy γ, as a function of $\Delta\mu$, is shown in Fig. 1a. The calculations are performed using slab models with dopants from trivalent, quadrivalent, and pentavalent elements (Sc–Ni) substituted at the octahedral site, and bivalent (Cu and Zn) at the tetrahedral site, as shown in the insets in Fig. 1b. All doping elements are found to decrease the surface energy. Among them, Ti doping results in the lowest surface energy. Cr doping also significantly reduces the surface energy compared to other elements, such as Fe, Mn, Zn, and Cu (inset in Fig. 1a).

Another indicator of stability is the dopant formation energy E_{f}, which quantifies the energetic cost of introducing dopant M into the slab and is calculated as

$$E_{\text{f}} = E_{\text{M-doped slab}} - E_{\text{pure slab}} - E_{\text{M}} + E_{\text{Co}} \tag{7}$$

Here, the energies of E_{M} and E_{Co} are calculated using a pure element. When $E_{\text{f}} < 0$, doping by replacing M on the Co site favors the thermodynamic stability. The calculated formation energies are presented in Fig. 1b and Table S3. Again, Ti has the lowest E_{f}. Although the Cr dopant has an E_{f} higher than Sc, Ti, and V, it is lower than those of all other dopants, indicating a relatively higher thermodynamic stability. The enhanced stability from doping with early TMs on the octahedral sites may

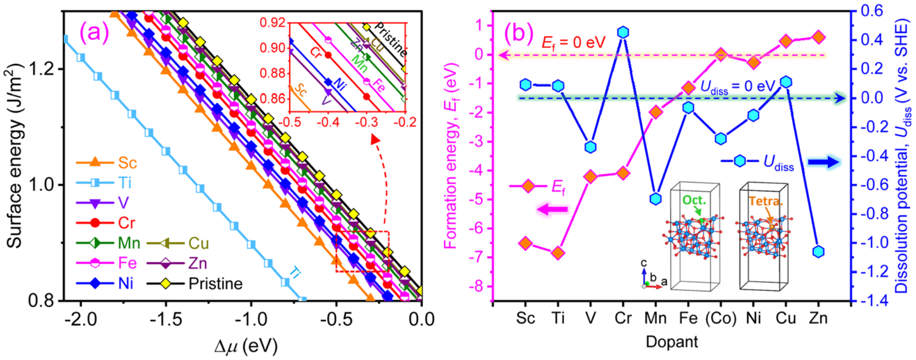

Fig. 1 (a) Surface energy as a function of oxygen chemical potential ($\Delta\mu$). (b) Formation energy E_f (pink, left axis) and dissolution potential U_{diss} (blue, right axis). Insets: two slab models with dopants on the octahedral and tetrahedral sites.

result from their relatively larger ionic sizes and lower electronegativities (Table S1), which reduce lattice distortion during the surface formation and strengthen the metal M–O bonds.

The electrochemical stability, evaluated by the dissolution potential U_{diss}, should also be taken into account.[51–53] The U_{diss} is expressed as

$$U_{diss} = U^0_{diss} - E_f/ne \tag{8}$$

where U^0_{diss} is the standard dissolution potential of the bulk metal, which can be found in the literature,[52] and n is the number of electrons involved in dissolution. When $U_{diss} > 0$ (*vs.* standard hydrogen electrode, SHE), it is considered electrochemically stable. The calculated results are presented in Fig. 1b and Table S3. It is found that only Sc-, Ti-, Cr-, and Cu-doped materials are electrochemically stable, with Cr showing the highest stability. Although Cr-doping produces a higher E_f compared with Sc, Ti, and V, its bulk standard dissolution potential of $U^0_{diss} = -0.91$ V is much higher than those of Sc (−2.08 V), Ti (−1.63 V), and V (−1.18 V), causing the highest U_{diss} value with enhanced electrochemical stability.

Next, we evaluate the OER activities of these dopants. The well-established adsorbate evolution mechanism (AEM) is employed to compute the OER free energies in an acidic environment as follows:[50,54,55]

$$\text{Step 1: } * + H_2O\ (l) \rightarrow {*OH} + H^+ + e^- \tag{9}$$

$$\Delta G_1 = (E_{*OH} + 0.5E_{H_2} - E_* - E_{H_2O}) + (\Delta ZPE - T\Delta S) - e\phi + k_BT\ln 10 \times pH \tag{10}$$

$$\text{Step 2: } {*OH} \rightarrow {*O} + H^+ + e^- \tag{11}$$

$$\Delta G_2 = (E_{*O} + 0.5E_{H_2} - E_{*OH}) + (\Delta ZPE - T\Delta S) - e\phi + k_BT\ln 10 \times pH \tag{12}$$

$$\text{Step 3: } {*O} + H_2O\ (l) \rightarrow {*OOH} + H^+ + e^- \tag{13}$$

$$\Delta G_3 = (E_{*OOH} + 0.5E_{H_2} - E_{*O} - E_{H_2O}) + (\Delta ZPE - T\Delta S) - e\phi + k_BT\ln 10 \times pH \tag{14}$$

$$\text{Step 4: } {*OOH} \rightarrow * + O_2\ (g) + H^+ + e^- \tag{15}$$

$$\Delta G_4 = 4.92 - \Delta G_1 - \Delta G_2 - \Delta G_3 \tag{16}$$

Here, * represents the active site of the catalyst; (l) and (g) denote the liquid and gas phases, respectively; ϕ is the external potential; and k_B is the Boltzmann constant. The zero-point energy (ZPE) and entropy correction ($T\Delta S$) values are listed in Table S4.[50,56,57]

The effective binding energies of the *O, *OH, and *OOH intermediates are calculated as follows:[57]

$$\Delta G_{*O} = (E_{*O} * E_* * E_{H_2O} + E_{H_2}) + (\Delta ZPE - T\Delta S) \tag{17}$$

$$\Delta G_{*OH} = (E_{*OH} - E_* - E_{H_2O} + 0.5E_{H_2}) + (\Delta ZPE - T\Delta S) \tag{18}$$

$$\Delta G_{*OOH} = (E_{*OH} - E_* - 2E_{H_2O} + 1.5E_{H_2}) + (\Delta ZPE - T\Delta S) \tag{19}$$

The calculation results are presented in Table S5.

A universal scaling relationship is found between ΔG_{*OOH} and ΔG_{*OH}, as illustrated in Fig. 2a. The regression line (solid) closely matches the ideal line (dotted), consistent with prior reports.[56] The free energy ΔG_i and binding energies of the four-step OER process are calculated with different dopants, as shown in Table S5, and the results for Cr-, Fe-, and Ni-doped systems and pristine Co_3O_4 are presented in Fig. 2b ($\phi = 0$ V), with overpotentials (η) indicated. The overpotentials of pristine and Cr-doped Co_3O_4 are calculated as 0.49 V and 0.36 V, which are close to the experimental results of 401 mV and 366 mV, respectively, as depicted in the following experimental section. The charge differences for the Cr-doped slabs are shown in the insets of Fig. 2b, and the details are provided in Fig. S2, where the Bader charge transfers are indicated.

Plotting the negative overpotential ($-\eta$) against the difference ($\Delta G_{*O} - \Delta G_{*OH}$) yields a volcano-type relationship, as shown in Fig. 2c. The two straight lines outlining the ideal volcano shape are calculated according to the scaling relationship as follows

$$\eta = \max[(\Delta G_{*O} - \Delta G_{*OH}), 3.14 - (\Delta G_{*O} - \Delta G_{*OH})]/e - 1.23 \tag{20}$$

where 3.14 is the intercept, as shown in Fig. 2a. The left leg location of the volcano (such as Mn) indicates strong binding to

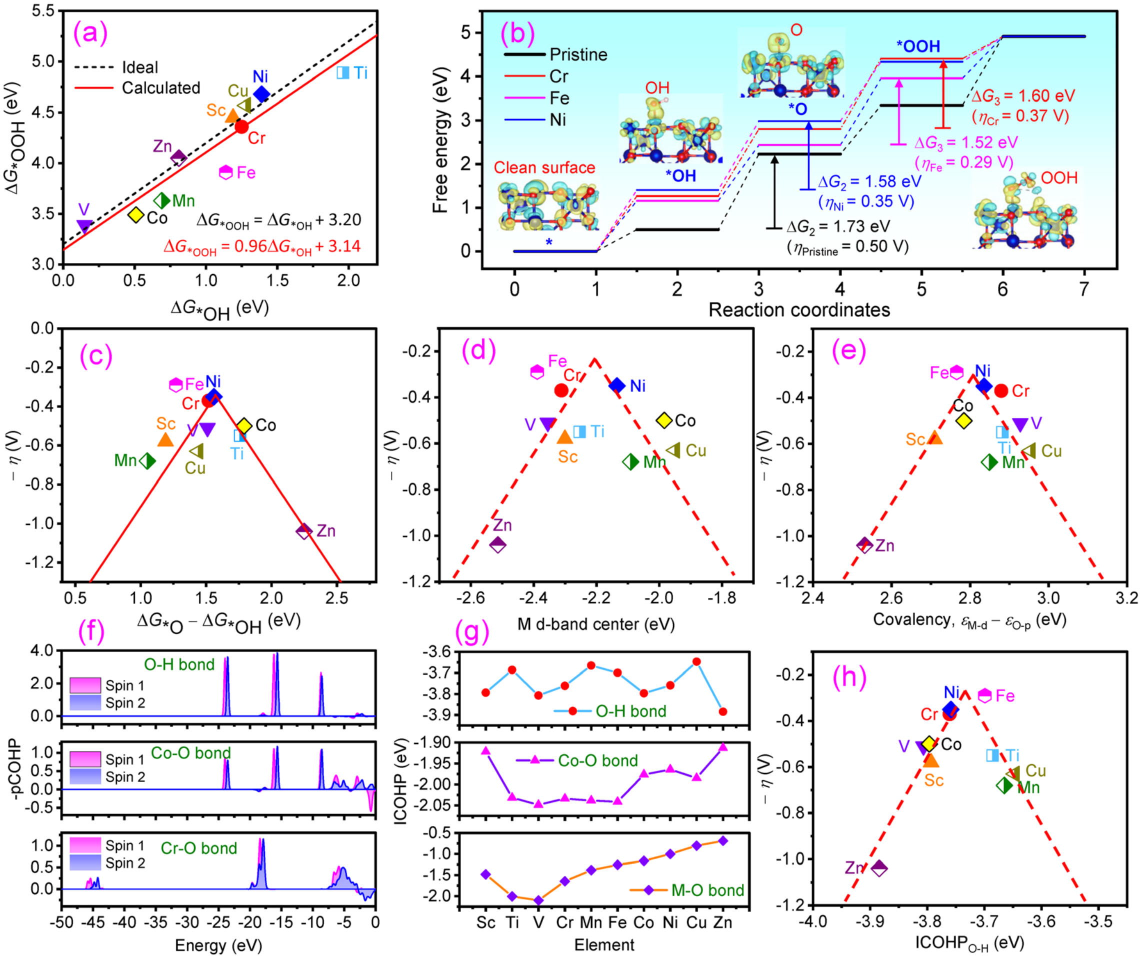

Fig. 2 (a) Scaling relationship between ΔG_{*OOH} and ΔG_{*OH} for various dopants. (b) Calculated free energy diagram during the OER without an external potential ($\phi = 0$ V). (c) Volcano plot of the negative overpotential as a function of $\Delta G_{*O} - \Delta G_{*OH}$. The dopants Ni, Fe, and Cr are located near the top of the plot. (d and e) Volcano plots of the negative overpotential as a function of the transition metal M (Co and dopant) 3d-band center and covalency, respectively. (f) Calculated pCOHP for the O–H, Co–O, and Cr–O bonds from the Cr-doped slab with *OOH. (g) Average ICOHP values of the O–H, Co–O, and Cr–O bonds for various doped systems. (h) Volcano plots of the negative overpotential as a function of ICOHP of the O–H bond. Dotted lines are drawn to guide the eye.

oxygen intermediates. In contrast, the right leg location indicates weak binding (such as Zn). Among the dopants, only Fe, Ni, and Cr exhibited high OER activity with low overpotentials. In contrast, Ti, V, and Sc show no significant impact on the overpotential compared to pristine Co_3O_4, whereas Mn, Cu, and Zn increase the overpotentials. Among Fe, Ni, and Cr, Fe exhibits the highest activity.

The transition metal d-band center (ε_d) is often used to describe adsorbate binding strength.[25,58] When the d-band center ε_d shifts to the Fermi level, a strong binding of the intermediates is anticipated, whereas when ε_d shifts away from the Fermi level, a weaker binding of the intermediates results.[59] We computed the metal d-band center ε_d and the O p-band center ε_p according to the following definition:

$$\varepsilon = \frac{\int E \times D(E)\mathrm{d}E}{\int D(E)\mathrm{d}E} \tag{21}$$

where E is the energy, and $D(E)$ is the density of states (DOS), calculated using DFT. The partial density of states (PDOS) curves for oxygen and metal M (including both Co and the dopant) are shown in Fig. S3, while the PDOS for oxygen and Co only are shown in Fig. S4. The calculated band centers and covalency values are presented in Table S6. A volcano-shaped relationship between $-\eta$ and ε_d is observed (Fig. 2d), indicating that a moderate ε_d, at approximately −2.2 eV, corresponds to the best catalytic performance. Here, ε_d includes contributions from both Co and the dopant. It is found that Zn has the lowest ε_d, with the weakest binding. Additionally, we calculated the covalency as the difference between the M 3d-band center ($\varepsilon_{M\text{-}d}$) and O 2p band center ($\varepsilon_{O\text{-}p}$). A plot of $-\eta$ *versus* covalency is shown in Fig. 2e, which also displays a volcano trend with an optimum value of approximately 2.8 eV. These results suggest that neither high nor low covalency is ideal; instead, moderate covalency is associated with lower overpotentials and enhanced OER activity. In contrast, when considering the Co 3d-band alone, the data deviate significantly from the volcano trend (Fig. S5). Therefore, the d-band center of metal M, comprising Co and the dopant, may serve as a better descriptor for catalytic performance than the Co d-band alone in revealing a volcano shape.

Bonding strength can also be evaluated from the integrated COHP (ICOHP) values.[60] The ICOHP is obtained by integrating the projected COHP (pCOHP) from low energy to the Fermi energy E_F as follows:

$$\mathrm{ICOHP} = \int_{-\infty}^{E_F} \mathrm{pCOHP}(E)\mathrm{d}E \tag{22}$$

We calculated the ICOHP of various doped systems to study the O–H bonding (for *OH and *OOH intermediates), the Co–O bonding between the active Co and intermediates (*O, *OH, and *OOH), and the M–O bonding of the dopant M (including Co for the pristine sample) with its neighboring O. The pCOHP of O–H, Co–O, and Cr–O are shown in Fig. 2f for the Cr-doped system with *OOH intermediate. The detailed results for *O, *OH, and *OOH are demonstrated in Fig. S6–S8, respectively. Note that the pCOHP axis is plotted with a negative sign. Negative values correspond to bonding (above the 0-axis), and positive values correspond to antibonding (below the 0-axis). The averaged ICOHP values for the O–H, Co–O, and M–O bonds are shown in Fig. 2g and Table S7. The ICOHP of O–H is shown at the top of Fig. 2g, where Cr, Fe, and Ni have intermediate ICOHP values, and when plotted with $-\eta$, their ICOHP locations are found to be optimal, exhibiting a volcano-like shape, centered at −3.73 eV, as shown in Fig. 2h. The area on the left leg, with a more negative ICOHP value, indicates stronger bonding. In the Zn-doped slab with *OOH, it is found that after geometrical optimization, the H atom moves away from the *OO intermediate and forms a bond with an O atom on the slab surface (Fig. S2), resulting in a stronger O–H bond than the others. The ICOHP values of Co–O and M–O are shown in the middle and bottom rows of Fig. 2g, respectively. The ICOHP of the M–O bond is overall consistent with the dopant formation energy after V, as shown in Fig. 1b. The relationships between the ICOHP of Co–O and M–O with $-\eta$ are shown in Fig. S9a and b, respectively. Their volcano shapes are not comparable to those of O–H bonds. Their bonding lengths are listed in Table S8 and Fig. S10(a–c). Again, the negative potential *vs.* O–H bond length shows a better volcano shape (Fig. S10d) than the Co–O (Fig. S10e) and M–O bond length (Fig. S10f).

Based on DFT calculations, although Fe and Ni doping can produce high theoretical activities, their doped systems exhibit substantially reduced stability in acidic media compared to the Cr-doped system, particularly a higher propensity for dissolution at anodic potentials. In contrast, Cr doping offers a more favorable balance between activity and robustness, and the calculated stability descriptors indicate suppressed cation dissolution relative to Fe- or Ni-doped systems. Given the stringent durability requirements for PEM anodes in acidic electrolytes, we therefore chose Cr-doped Co_3O_4 for experimental validation as a compromise that preserves high intrinsic activity while markedly improving structural stability.

3.2 Experimental results and discussion

We selected Cr for this experimental study and synthesized Cr-doped Co_3O_4 nanoparticles using a modified, scalable Pechini method at 400 °C. Fig. 3a illustrates the X-ray diffraction (XRD) patterns of pristine Co_3O_4 and Co_3O_4 doped with chromium at varying concentrations from 5% to 30%. The XRD patterns of all the samples exhibit peaks corresponding to the cubic spinel structure, with the space group $Fd\bar{3}m$. As the Cr doping concentration increases, the peak intensity decreases and broadens, indicating that the introduction of Cr atoms induces strain and defects within the Co_3O_4 matrix. Fig. 3b presents the high-resolution transmission electron microscopy (HR-TEM) analysis of the 10% Cr-doped sample. It reveals that the nanoparticles are highly crystalline, with an average diameter of 13.8 nm. The inset in Fig. 3b shows an energy-dispersive spectroscopy (EDS) analysis, confirming the presence of Co, O, and Cr elements, along with a Cu peak from the TEM grid. Fig. 3c illustrates the selected-area electron diffraction (SAED) pattern, which shows sharp diffraction rings from the polycrystals. The inset in Fig. 3c depicts the electron diffraction intensity profile along the radial distribution,[61] providing a detailed quantitative analysis comparable to that of the XRD pattern in Fig. 3a. A high-angle annular dark-field (HAADF) image is presented in Fig. 3d, and the Co, O, and Cr elemental maps are presented in Fig. 3e–g, respectively. These elements are uniformly distributed throughout the sample, indicating the successful incorporation of Cr into the Co_3O_4 lattice. The uniform distribution of Cr is crucial for maintaining the structural and functional integrity of catalysts.

X-ray photoelectron spectroscopy (XPS) survey shows peaks corresponding to Co 2p, Cr 2p, O 1s, and C 1s (Fig. 4a). The presence of Cr 2p peaks confirms the incorporation of chromium. The binding energy positions suggest that Cr and Co coexist in a mixed oxidation state. Fig. 4b and c show the high-resolution XPS spectra of Co 2p in pristine Co_3O_4 and 10% Cr–Co_3O_4, respectively. In both cases, the Co $2p_{3/2}$ peak appears at approximately 780 eV, corresponding to the Co^{3+} and Co^{2+} oxidation states. Further deconvolution reveals that the peaks at ~779.8 eV and ~780.6 eV correspond to Co^{3+}, whereas the peaks at ~782 eV correspond to Co^{2+}. A broad satellite peak (~786–788 eV), characteristic of Co^{2+}, is also observed. A comparison between Fig. 4b and c shows slight changes in the peak positions and intensities, indicating electronic interactions between Cr and Co. Fig. 4d shows the high-resolution XPS of Cr 2p (10% Cr–Co_3O_4). The Cr $2p_{3/2}$ peak is deconvoluted into Cr^{3+} (~576.3 eV & ~577.2 eV), associated with Cr_2O_3-like species, and Cr^{6+} (~579.2 eV), attributed to CrO_3 or surface chromate species. The presence of both Cr^{3+} and Cr^{6+} suggests the existence of mixed oxidation states, possibly due to the surface oxidation of the chromium species. Fig. 4e and f show the high-resolution XPS spectra of O 1s in pristine Co_3O_4 and 10% Cr–Co_3O_4, respectively. Deconvolution of the O 1s spectrum reveals lattice oxygen (~529.6 eV) from the metal oxides, and surface oxygen (~531.5–532.5 eV), which may correspond to hydroxyl or adsorbed oxygen species. The higher intensity of surface oxygen (Fig. 4f) compared to that in Fig. 4e suggests an enhanced

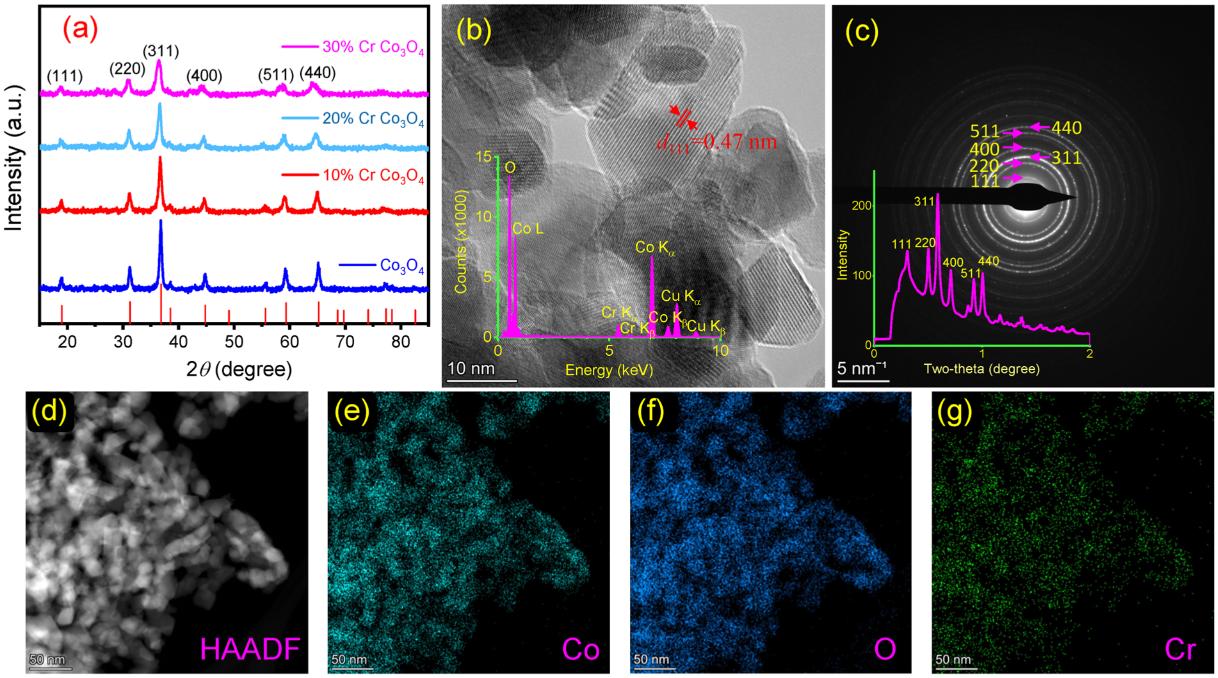

Fig. 3 (a) XRD. (b) HRTEM image of 10% Cr-doped Co_3O_4 (inset: EDS analysis). (c) SAED pattern (inset: quantitative electron diffraction intensity profile). (d–g) HAADF image and elemental maps of Co, O, and Cr.

availability of oxygen species, which is beneficial for catalytic applications.

Fig. 5a shows the linear sweep voltammetry (LSV) curves, which reveal the catalytic activity of Cr-doped Co_3O_4 by measuring the current density as a function of the applied potential. The 10% Cr-doped Co_3O_4 exhibits the lowest overpotential (366 mV @ 10 mA cm^{-2}), indicating superior OER activity. The other compositions exhibit higher overpotentials:

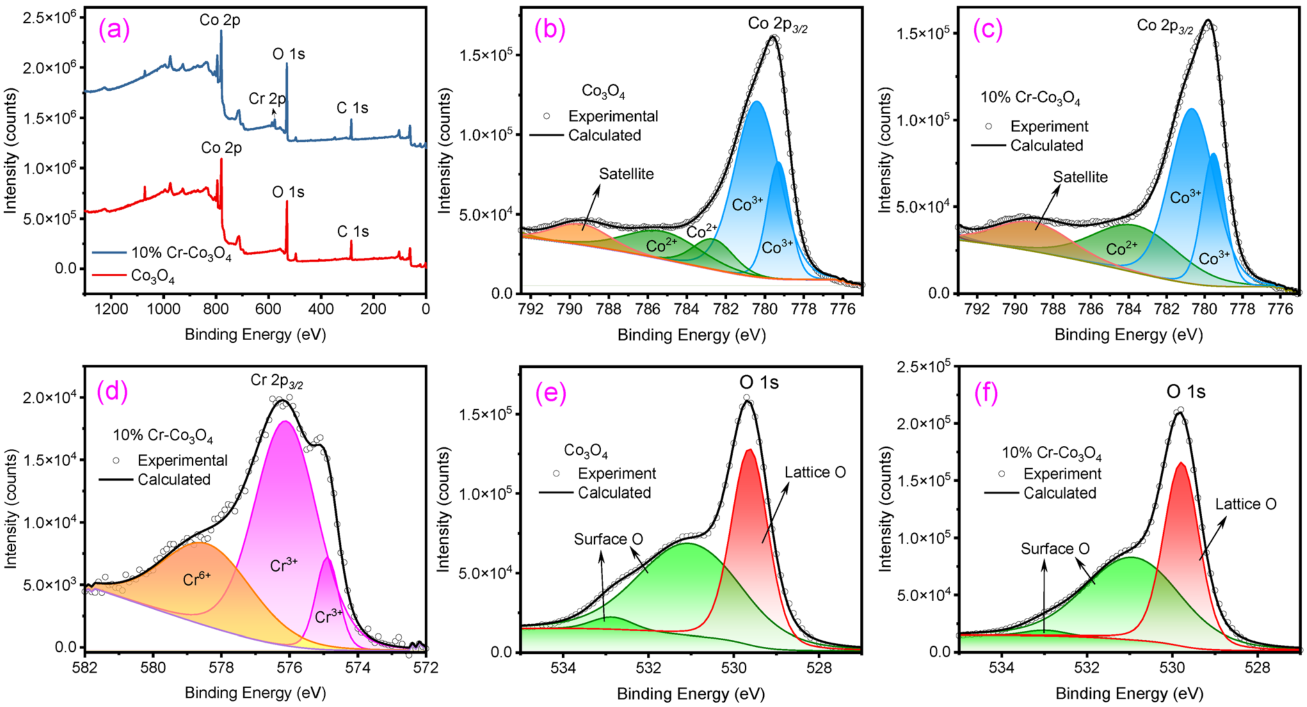

Fig. 4 (a) XPS survey spectra of 10% Cr-doped Co_3O_4 and pristine Co_3O_4. (b and c) High-resolution XPS spectra of Co $2p_{3/2}$ of pristine Co_3O_4 (b) and 10% Cr–Co_3O_4 (c). (d) High-resolution XPS spectra of Cr $2p_{3/2}$ of 10% Cr–Co_3O_4. (e and f) High-resolution XPS spectra of O 1s of pristine Co_3O_4 (e) and 10% Cr–Co_3O_4 (f).

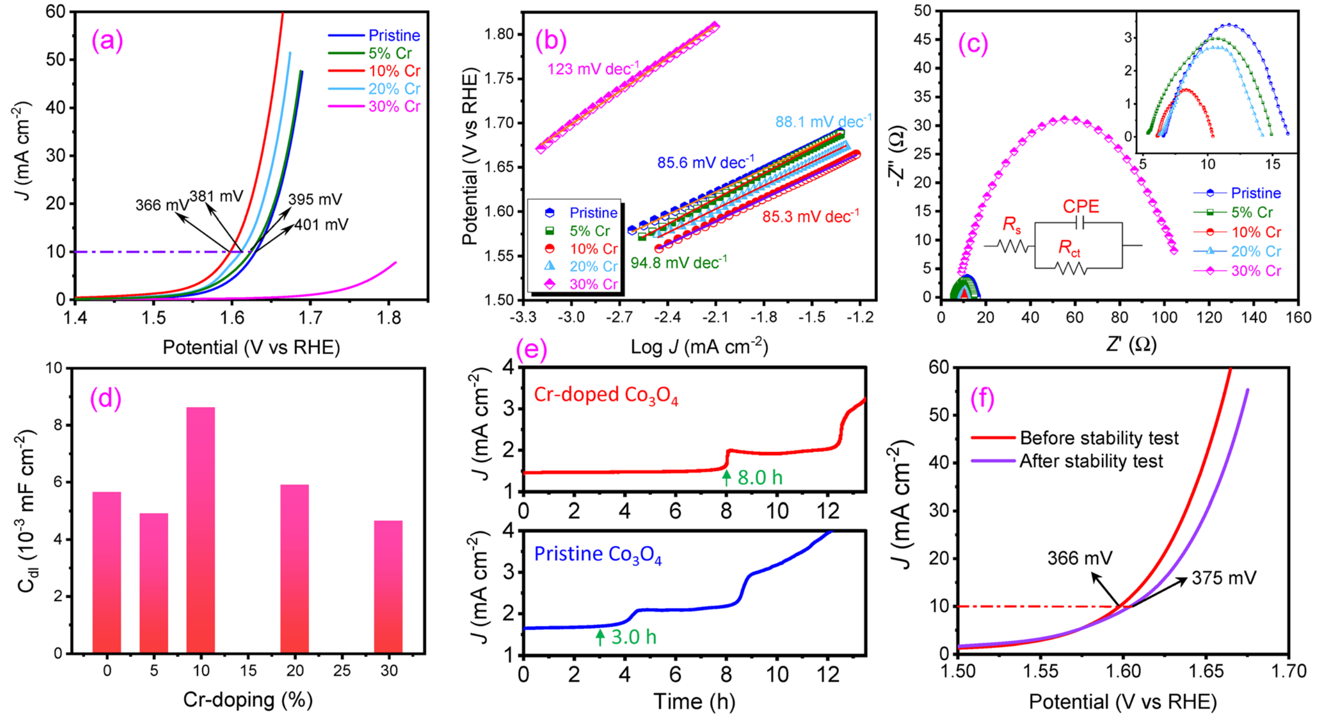

Fig. 5 LSV curves (a), Tafel slopes (b), EIS analysis (c), and double-layer capacitance (d) of pristine and Cr-doped Co_3O_4. (e) Stability test of 10% Cr-doped Co_3O_4 (top) and pristine Co_3O_4 (bottom). (f) Comparison of LSV curves before and after the stability test.

5% Cr (381 mV), 20% Cr (395 mV), pristine (401 mV), and 30% Cr (>401 mV). The Tafel slopes of pristine and Cr-doped Co_3O_4 are shown in Fig. 5b, and among them, 10% Cr–Co_3O_4 has the lowest Tafel slope (85.6 mV dec^{-1}). Pristine Co_3O_4 exhibits a higher Tafel slope (94.8 mV dec^{-1}), and 30% Cr–Co_3O_4 shows the highest Tafel slope (123 mV dec^{-1}). The lower Tafel slope of 10% Cr–Co_3O_4 suggests more efficient electron transfer, leading to faster OER kinetics, whereas excessive Cr (30%) negatively impacts conductivity and catalytic activity. The results are consistent with the computational results, which show that Cr decreases the overpotential from 490 mV to 360 mV. In the literature, Cr has been reported to reduce the overpotential from 420 mV to 350 mV while increasing the Tafel slope from 52 to 60 mV dec^{-1} in 1 M NaOH.[23] In another report, Cr reduced the overpotential from 385 mV to 333 mV and the Tafel slope from 84 to 79 mV dec^{-1} in 0.5 M H_2SO_4.[40]

The EIS Nyquist plots are used to measure the charge-transfer resistance (R_{ct}) of the pristine and Cr-doped Co_3O_4 catalysts at the electrode–electrolyte interface (Fig. 5c). The 10% Cr–Co_3O_4 catalyst shows the smallest semicircle, indicating the lowest R_{ct} value. In comparison, 30% Cr–Co_3O_4 has the highest R_{ct} value. This suggests that 10% Cr doping optimizes electron transport, whereas excess Cr increases resistance and decreases catalytic performance. The higher value for the 30% Cr sample confirms its higher bulk resistivity, likely due to excessive doping that creates charge-carrier scattering or forms insulating phases, consistent with its poorer overall OER performance shown in Fig. 5a. Further, Fig. 5d shows the double-layer capacitance (C_{dl}) of the pristine and Cr-doped catalysts. The 10% Cr–Co_3O_4 sample exhibits the highest C_{dl} value, indicating the presence of the largest electrochemically active surface area (ECSA) and the greatest number of electrochemically active sites. The other catalysts have lower C_{dl} values, suggesting a low ECSA and blocking of active sites. We further normalized the current density to the ECSA, and the performance trend remains unchanged. At η = 370 mV (1.6 V *vs.* RHE in 0.5 M H_2SO_4), the 10% Cr sample delivers an ECSA-normalized current density of $J_{ECSA} = 1.8$ mA $cm_{ECSA}{}^{-2}$, while the other samples show lower values. Therefore, the improved activity of the 10% Cr sample is not solely due to its increased surface area (Fig. S11), suggesting that the Co sites are more intrinsically active.

The stability test is shown in Fig. 5e. The Cr-doped Co_3O_4 exhibits stable performance at 0.5 mA current for up to 8.0 h, while the pristine Co_3O_4 remains stable for only up to 3.0 h. Cr doping prolongs the stability by a factor of 2.7. LSV was also conducted using the sample after stability testing. As shown in Fig. 5f, following the long-term stability test, the overpotential increases by only 11 mV, indicating the high stability of the doped material. After a 24 h long-term stability test, the sample on carbon cloth used as the working electrode was analyzed by XRD, as shown in Fig. 6. The carbon peak is from the carbon cloth, and Co_3O_4 is still the primary phase, while oxides with other oxidation states of Co_2O_3, CoO, and CoO_2 can also be identified. The appearance of these oxides results in the deterioration of the OER activities, as shown in Fig. 5f, where the overpotential increased from 366 to 375 mV at 10 mA cm^{-2}, indicating that Co_3O_4 appears to be the most catalytically active oxide in this cobalt oxide system.

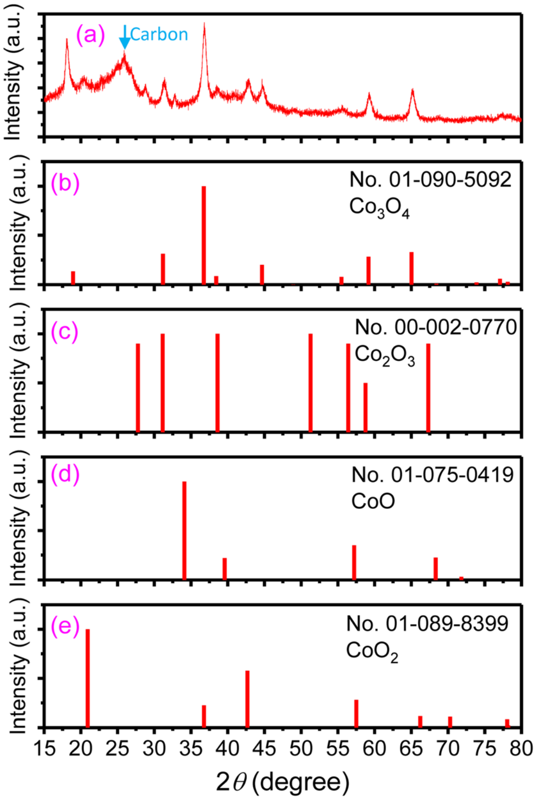

Fig. 6 XRD pattern of the electrode sample after long-term durability test (a), compared with the standards of Co_3O_4 (b), Co_2O_3 (c) CoO (d), and CoO_2 (e).

4 Conclusions

In summary, we employed DFT to systematically investigate the effects of doping Co_3O_4 with fourth-row TMs ranging from Sc to Zn. Computational screening shows that early TMs enhance the thermodynamic stability of the host oxide, with Ti providing the best thermodynamic stabilization and Cr affording the highest electrochemical stability. As a kinetic descriptor, the d-band center, when considering both Co and the dopant metal, outperformed the Co-only d-band center, exhibiting a volcano-type dependence of the OER activity. Optimal performance occurs at a moderate d-band center (~ -2.2 eV) and moderate covalency (~ 2.8 eV); values that are either too high or too low in either metric degrade the activity. Bonding analysis further indicated that the ICOHP of the O–H bond was a more effective activity descriptor (centered at -3.73 eV) than the ICOHP of the Co–O or M–O bonds. These metrics, including the d-band center, covalency, and ICHOP, can guide catalyst searches.

Among the screened elements, Cr emerged as the most promising dopant, balancing the structural stability and catalytic activity. Guided by these computational insights, we experimentally evaluated Cr-doped Co_3O_4 under acidic OER conditions. The 10% Cr-doped catalyst demonstrated outstanding performance, achieving an overpotential of 366 mV at 10 mA cm^{-2} in 0.5 M H_2SO_4. Additionally, Cr incorporation significantly improved durability, extending the catalyst's operational lifetime by a factor of 2.7, with only a minimal increase in overpotential (11 mV) after extended testing. Overall, this study establishes a generalizable computational–experimental framework for identifying and validating dopants that enhance the activity and longevity of oxide electrocatalysts for acidic water oxidation.

Author contributions

S. R. Ede conducted sample synthesis, XPS, and electrochemical measurements and prepared part of the draft; H. M. Paige participated in sample synthesis; J. Wu and S. Han participated in electrochemical measurements; C. M. Adhikari participated in the DFT; A. S. Kumbhar conducted TEM; and Z. Luo designed and supervised the project, conducted DFT, analyzed the data, and prepared the manuscript.

Conflicts of interest

The authors declare that they have no competing financial interests.

Data availability

All data are available upon request from the corresponding author.

The data supporting this article are available in the supplementary information (SI). Supplementary information: additional detailed parameters for computation; Lobster input file; calculated formation energy and dissolution potential; ZPE and $T\Delta S$ values; calculated binding energies of the *O, *OH, and *OOH intermediates; O 2p-band and metal M (dopant and Co) 3d-band centers and associated covalencies; calculated ICHOP values of O–H, Co–O, and M–O bonds; calculated O–H, Co–O, and M–O bond lengths; schematic sample synthesis; figures of calculated charge differences of slabs attached with *OH, *O, and *OOH; figures of PDOS; calculated volcano plot of $-\eta$ *vs.* Co d-band center and covalency; calculated pCOHP of M-doped slabs with *O, *OH, and *OOH; calculated $-\eta$ *vs.* ICOHP of Co–O and M–O bonds; calculated bond length and $-\eta$ *vs.* bond lengths of O–H, Co–O, and M–O bonds; and ECSA normalized LSV curves of pristine and Cr-doped Co_3O_4. See DOI: https://doi.org/10.1039/d5ta08166a.

Acknowledgements

This initial research was supported by the National Science Foundation (NSF) under grant no. DMR 1827731. Recent work, following the DMR grant, was supported by NSF OIA 2430295 and NSF EES 2106181.

References

1 Y. Yan, B. Lin, L. Zhang, Y. Wang, H. Zhang, H. Zheng, T. Zhou, Y. Zhan, Z. Yu, Y. Kuang and J. Tang, *Chem. Eng. J.*, 2024, **487**, 150447.

2 N. Kousar, G. Patil, A. C. Kumbara, B. Nisty, G. H. Rajesh and L. K. Sannegowda, *Dalton Trans.*, 2025, **54**, 12714–12736.

3 Y. Liu, L. Li, X. Li, Y. Xu, D. Wu, T. Sakthivel, Z. Guo, X. Zhao and Z. Dai, *Sci. Adv.*, 2025, **11**, eads0861.

4 K. M. Naik, K. Hashisake, E. Higuchi and H. Inoue, *Mater. Adv.*, 2023, **4**, 561–569.

5 K. M. Naik and S. Sampath, *Electrochim. Acta*, 2018, **292**, 268–275.

6 M. Kıstı, B. Hüner, A. Albadwi, E. Özdoğan, İ. N. Uzgören, S. Uysal, M. Conağası, Y. O. Süzen, N. Demir and M. F. Kaya, *ACS Omega*, 2025, **10**, 9824–9853.

7 N. Wang, H. Xiang, L. Meng, C. Tang, Z. Dong, Y. Yang, L. Du and S. Ye, *Renewable Energy Syst. Equip.*, 2025, **1**, 61–66.

8 Y. Lin, Y. Dong, X. Wang and L. Chen, *Adv. Mater.*, 2023, **35**, 2210565.

9 C. Rong, K. Dastafkan, Y. Wang and C. Zhao, *Adv. Mater.*, 2023, **35**, 2211884.

10 Y. Zhou, H. Zhong, S. Chen, G. Wen, L. Shen, Y. Wang, R. Chen, L. Tao and S. Wang, *Carbon Energy*, 2025, **7**, e629.

11 Y. Cui, Y. Zhao, Z. Han, Z. Wang, W. Li, Y. Zhang, Z. Li, W. Wang and X. Fu, *J. Mater. Chem. A*, 2025, **13**, 17214–17241.

12 Q. Wu, Y. Wang, K. Zhang, Z. Xie, K. Sun, W. An, X. Liang and X. Zou, *Mater. Chem. Front.*, 2023, **7**, 1025–1045.

13 W. Feng, B. Chang, Y. Ren, D. Kong, H. B. Tao, L. Zhi, M. A. Khan, R. Aleisa, M. Rueping and H. Zhang, *Adv. Mater.*, 2025, **37**, 2416012.

14 A. A. Zasypkina, N. A. Ivanova, D. D. Spasov, R. M. Mensharapov, M. V. Sinyakov and S. A. Grigoriev, *Catalysts*, 2024, **14**, 303.

15 N. Mushtaq, H. M. N. Ullah, K. Aslam, M. Sufyan, Alamgir, M. Ali, M. Saleem, Q. Qiu, Y. Bin and M. Hussain, *Sustain. Mater. Technol.*, 2025, **46**, e01743.

16 H. Li, S. Wang and C. Zhao, *Aust. J. Chem.*, 2025, **78**, CH25104.

17 C. Rong, Q. Sun, J. Zhu, H. Arandiyan, Z. Shao, Y. Wang and Y. Chen, *Adv. Sci.*, 2025, **12**, e09415.

18 J. Swaminathan, A. B. Puthirath, M. R. Sahoo, S. K. Nayak, G. Costin, R. Vajtai, T. Sharifi and P. M. Ajayan, *ACS Appl. Mater. Interfaces*, 2019, **11**, 39706–39714.

19 S. L. Zhang, B. Y. Guan, X. F. Lu, S. Xi, Y. Du and X. W. D. Lou, *Adv. Mater.*, 2020, **32**, 2002235.

20 S. R. Ede, C. N. Collins, C. D. Posada, G. George, H. Wu, W. D. Ratcliff, Y. Lin, J. Wen, S. Han and Z. Luo, *ACS Catal.*, 2021, **11**, 4327–4337.

21 P. Guo, L. Shi, D. Liu, X. Wang, F. Gao, Y. Ha, J. Yin, M. Liu, H. Pan and R. Wu, *Mater. Today Catal.*, 2023, **1**, 100002.

22 L. Li, Q. Xu, Y. Zhang, J. Li, J. Fang, Y. Dai, X. Cheng, Y. You and X. Li, *J. Alloys Compd.*, 2020, **823**, 153750.

23 C.-C. Lin and C. C. L. McCrory, *ACS Catal.*, 2017, **7**, 443–451.

24 S. Banerjee, S. Debata, R. Madhuri and P. K. Sharma, *Appl. Surf. Sci.*, 2018, **449**, 660–668.

25 X. Wu, Z. Shao, Q. Zhu, X. Hou, C. Wang, J. Zeng, K. Huang and S. Feng, *ACS Catal.*, 2024, **14**, 5888–5897.

26 X. Yang, H. Li, A.-Y. Lu, S. Min, Z. Idriss, M. N. Hedhili, K.-W. Huang, H. Idriss and L.-J. Li, *Nano Energy*, 2016, **25**, 42–50.

27 J. S. Mondschein, J. F. Callejas, C. G. Read, J. Y. C. Chen, C. F. Holder, C. K. Badding and R. E. Schaak, *Chem. Mater.*, 2017, **29**, 950–957.

28 C. Rong, Q. Sun, J. Zhu, H. Arandiyan, Z. Shao, Y. Wang and Y. Chen, *Adv. Sci.*, 2025, **12**, e09415.

29 S. R. Ede and Z. Luo, *J. Mater. Chem. A*, 2021, **9**, 20131–20163.

30 Y. Zhu, J. Wang, T. Koketsu, M. Kroschel, J.-M. Chen, S.-Y. Hsu, G. Henkelman, Z. Hu, P. Strasser and J. Ma, *Nat. Commun.*, 2022, **13**, 7754.

31 Y. Xie, Y. Su, H. Qin, Z. Cao, H. Wei, F. Wu and G. Ou, *Int. J. Hydrog. Energy*, 2023, **48**, 14642–14649.

32 Z. Bai, L. Li, P. Yin and T. Lei, *Int. J. Hydrog. Energy*, 2025, **128**, 76–84.

33 R. Madhu, A. Karmakar, P. Arunachalam, J. Muthukumar, P. Gudlur and S. Kundu, *J. Mater. Chem. A*, 2023, **11**, 21767–21779.

34 Y. Yang, Y. Xu, H. Liu, Q. Zhang, B. Liu, M. Yang, H. Dai, Z. Ke, D. He, X. Feng and X. Xiao, *Nano Res.*, 2024, **17**, 5922–5929.

35 S. Zuo, Z.-P. Wu, D. Xu, R. Ahmad, L. Zheng, J. Zhang, L. Zhao, W. Huang, H. Al Qahtani, Y. Han, L. Cavallo and H. Zhang, *Nat. Commun.*, 2024, **15**, 9514.

36 J. Zhang, G. Chen, D. Sun, Y. Tang, W. Xing, H. Sun and X. Feng, *Chem. Sci.*, 2024, **15**, 17900–17911.

37 K.-L. Yan, J.-F. Qin, J.-H. Lin, B. Dong, J.-Q. Chi, Z.-Z. Liu, F.-N. Dai, Y.-M. Chai and C.-G. Liu, *J. Mater. Chem. A*, 2018, **6**, 5678–5686.

38 X. Cheng, Y. Liu, Y. Shang, N. Han, G. He and Z. Xu, *Ionics*, 2024, **30**, 3391–3401.

39 T. Wang, Y. Shi, J. Fei, J. Zhu, L. Song, C. Li, T. Zhan, J. Lai and L. Wang, *Appl. Catal. B Environ. Energy*, 2024, **358**, 124367.

40 Q. Yan, J. Feng, W. Shi, W. Niu, Z. Lu, K. Sun, X. Yang, L. Xue, Y. Liu, Y. Li and B. Zhang, *Adv. Sci.*, 2024, **11**, 2402356.

41 L.-Y. Chueh, Y.-W. Hsu, Z.-W. Wang, H.-C. Lin, S.-Y. Hung, Y.-L. Chen, H.-Y. Chen and Y.-T. F. Pan, *Electrochim. Acta*, 2024, **497**, 144575.

42 G. Kresse and J. Furthmüller, *Comput. Mater. Sci.*, 1996, **6**, 15–50.

43 G. Kresse and J. Furthmüller, *Phys. Rev. B:Condens. Matter Mater. Phys.*, 1996, **54**, 11169–11186.

44 P. E. Blöchl, *Phys. Rev. B:Condens. Matter Mater. Phys.*, 1994, **50**, 17953–17979.

45 J. P. Perdew, K. Burke and M. Ernzerhof, *Phys. Rev. Lett.*, 1996, **77**, 3865–3868.

46 S. L. Dudarev, G. A. Botton, S. Y. Savrasov, C. J. Humphreys and A. P. Sutton, *Phys. Rev. B:Condens. Matter Mater. Phys.*, 1998, **57**, 1505–1509.

47 Y. Feng, Y. Chen, L. Zheng, X. Chen, T. Li and W. Zhao, *iScience*, 2025, **28**, 113080.

48 R. Nelson, C. Ertural, J. George, V. L. Deringer, G. Hautier and R. Dronskowski, *J. Comput. Chem.*, 2020, **41**, 1931–1940.

49 S. Selcuk and A. Selloni, *J. Phys. Chem. C*, 2015, **119**, 9973–9979.

50 Y. Peng, H. Hajiyani and R. Pentcheva, *ACS Catal.*, 2021, **11**, 5601–5613.

51 J. Greeley and J. K. Nørskov, *Electrochim. Acta*, 2007, **52**, 5829–5836.

52 X. Guo, J. Gu, S. Lin, S. Zhang, Z. Chen and S. Huang, *J. Am. Chem. Soc.*, 2020, **142**, 5709–5721.

53 T. Priamushko, E. Franz, A. Logar, L. Bijelić, P. Guggenberger, D. Escalera-López, M. Zlatar, J. Libuda, F. Kleitz, N. Hodnik, O. Brummel and S. Cherevko, *J. Am. Chem. Soc.*, 2025, **147**, 3517–3528.

54 Z. Luo, *J. Mater. Chem. A*, 2025, **13**, 2537–2573.

55 S. Ram, A. S. Lee, S.-C. Lee and S. Bhattacharjee, *Chem. Mater.*, 2025, **37**, 3608–3621.

56 I. C. Man, H.-Y. Su, F. Calle-Vallejo, H. A. Hansen, J. I. Martínez, N. G. Inoglu, J. Kitchin, T. F. Jaramillo, J. K. Nørskov and J. Rossmeisl, *ChemCatChem*, 2011, **3**, 1159–1165.

57 P. Liao, J. A. Keith and E. A. Carter, *J. Am. Chem. Soc.*, 2012, **134**, 13296–13309.

58 W. Qu, Z. Tang, S. Tang, H. Wen, J. Fang, Q. Lian, D. Shu and C. He, *Adv. Funct. Mater.*, 2023, **33**, 2301677.

59 S. Jiao, X. Fu and H. Huang, *Adv. Funct. Mater.*, 2022, **32**, 2107651.

60 S. Steinberg and R. Dronskowski, *Crystals*, 2018, **8**, 225.

61 Z. Luo, *A Practical Guide to Transmission Electron Microscopy, Volume II: Advanced Microscopy*, Momentum Press, New York, NY, 2016.